

Gyrokinetic simulations of ETG and ITG turbulence

A.M. Dimits¹, W.M. Nevins¹, D.E. Shumaker¹, G.W. Hammett²,
T. Dannert³, F. Jenko³, M.J. Pueschel³, W. Dorland⁴,
S.C. Cowley⁵, J.N. Leboeuf⁵, T.L. Rhodes⁵, J. Candy⁶ and
C. Estrada-Mila⁷

¹ Lawrence Livermore National Laboratory, Livermore, CA 94550, USA

² Princeton Plasma Physics Laboratory, Princeton, NJ 08536, USA

³ Max Planck Institut für Plasmaphysik, Garching 85748, Germany

⁴ University of Maryland, College Park, MD 20742, USA

⁵ University of California, Los Angeles, CA 90095-1547, USA

⁶ General Atomics, San Diego, CA 92186, USA

⁷ University of California, San Diego, CA 92186, USA

E-mail: dimits1@llnl.gov

Received 10 January 2007, accepted for publication 23 May 2007

Published 23 July 2007

Online at stacks.iop.org/NF/47/817

Abstract

We report on the resolution of a significant discrepancy between published continuum-code simulations and subsequent global particle-in-cell (PIC) simulations of electron-temperature-gradient (ETG) turbulence. Our investigations, using gyrokinetic δf -PIC- and continuum-code simulations and analytical theory, strongly support the conclusion from the earlier continuum-code simulations that ETG turbulence can drive the electron thermal conductivity χ_e large enough to be significant in some tokamaks. A successful ETG-turbulence benchmark between δf -PIC and continuum codes for ETG turbulence has also been completed. Scans in the magnetic shear show an abrupt transition to a high- χ_e state as the shear is increased from the benchmark value of $s = 0.1$ to above $s = 0.4$. When nonadiabatic ions are used, this abrupt transition is absent, and χ_e reaches values consistent with transport analyses of DIII-D, JET, JT60-U and NSTX discharges. The balances of zonal-flow driving and damping terms in late-time quasi-steady phase of ITG turbulence have been unfolded using a new run-time gyrokinetic-simulation diagnostic. The zonal flow level is set by a balance of large driving and damping terms which almost cancel each other. The driving is found to be mostly by the Reynolds stress, while the dissipation is mostly by the linear (transit-time) damping terms. It is also shown that useful zonal-flow-balance information can be obtained with spatially localized samples at as few as four poloidal locations. Real-geometry simulations have been undertaken, using the nonlinear δf -PIC gyrokinetic code SUMMIT/PG3EQ_NC, of the DIII-D ‘Cyclone’ shot #81499 and of shot #118561, which had broad-wavenumber-range density fluctuation measurements. Real geometry is found to have a significant effect on the transport rates, even though the effect on the linear growth rates is often modest.

PACS numbers: 52.65.Tt, 52.35.Ra, 52.25.Fi

(Some figures in this article are in colour only in the electronic version)

1. Introduction

We report on (1) the resolution of disparities between published continuum [1, 2] and particle-in-cell (PIC) [3, 4] nonlinear gyrokinetic simulations of toroidal electron-temperature-gradient (ETG) turbulence, (2) analysis of sources and sinks of zonal flow in ion-temperature-gradient (ITG) turbulence and (3) real-geometry simulation of ITG turbulence.

Gyrokinetic continuum-code simulations of ETG turbulence have indicated a sufficiently large value of the electron

thermal conductivity χ_e to be potentially significant in tokamaks [1, 2]. This was cast into doubt by more recent PIC simulations [3, 4] which, using similar plasma parameters, gave significantly lower values of χ_e . The differences between [1, 2] and [3, 4] were attributed to insufficient phase-space resolution and novel physics associated with global geometry [3, 4]. References [1] and [2] also differ from [3] and [4] in that magnetically trapped particles are eliminated in [1] and [2] ($r/R = 0$, where r and R are, respectively, the minor and major radii), but retained in [3] and [4] ($r/R = 0.18$). In section 2,

we summarize investigations of the above discrepancy that we have carried out [5, 6], using gyrokinetic simulations complemented by analytical theory, of the proposed explanations and of the more general question of whether ETG turbulence can be important in tokamaks.

Anomalous ion thermal transport in some tokamak discharges [7] is believed to be caused by toroidal ITG and related turbulence. There is now widespread evidence from simulations (see e.g. [8–10]) that zonal flows are a key component in the dynamics of such turbulence. For example, differences in zonal-flow dynamics account for the large difference in normalized transport values between ITG and ETG turbulence [1, 2]. (Here, the normalization is to the respective ‘gyroBohm’ level $\chi_{iGB} = v_{Ti} \rho_i^2 / L_{Ti}$ for ITG turbulence, and $\chi_{eGB} = v_{Te} \rho_e^2 / L_{Te}$ for ETG turbulence, where v_{Ti} and v_{Te} are the ion and electron thermal velocities, ρ_i and ρ_e are the ion and electron thermal gyroradii, and L_{Ti} and L_{Te} are the ion and electron temperature scale lengths.) Several studies to date have addressed the initial generation of zonal flows [11] and the stability of idealized zonal-flow states [12] in ITG turbulence. However, information on the relative importance of different driving and damping mechanisms in the late-time quasi-steady state would greatly add to the understanding of the turbulence-zonal-flow system and is directly accessible in simulations. We have therefore developed a run-time gyrokinetic-simulation diagnostic to extract this information, which has enabled us to unfold the balances of zonal-flow driving and damping terms in late-time quasi-steady ITG turbulence. This diagnostic and its application are discussed in section 3.

Our zonal-flow-balance diagnostic is similar in approach to work by Scott [13] and by Hallatschek and Zeiler [14]. Scott [13] addressed zonal flows in electromagnetic drift turbulence using a decomposition of the sources and sinks of zonal flow both by physical term and wavenumber. Our diagnostic is integral in wavenumber. A wavenumber decomposition of the sources and sinks in our ITG and ETG simulations will be presented in future work. Hallatschek and Zeiler [14] examined zonal flow sources and sinks in drift wave turbulence with a real-space diagnostic which is similar in spirit to ours, but further decomposes the zonal-field sources into a zero-frequency modal component and a geodesic-acoustic-mode (GAM) component. An approximate analogue of this diagnostic may be possible for our kinetic simulations, but is less straightforward than for the fluid system considered in [14]. Reference [14] also focused on terms that were useful for the identification of a $V_{||}$ instability as the mechanism for tertiary instability of the zonal flows in the tokamak-edge-relevant regime considered there.

Real tokamak discharge cross sections have significant departures from circularity due to intentional distortions (e.g. elongation and triangularity) and the proximity of divertor X points. This has motivated the development of SUMMIT/PG3EQ_NC, a real-geometry version of the gyrokinetic code PG3EQ [10]. Some results of applications of SUMMIT/PG3EQ_NC are presented in section 4.

The simulations shown and discussed in this work are collisionless. While collisions have been shown to be potentially important for ITG turbulence, especially in regimes where collisions damp otherwise undamped zonal flows which

strongly limit the transport [15], the effect of collisions is much more modest in cases such as those presented here, where there is robust transport in the absence of collisions.

Conclusions and discussion of the results of this work are presented in section 5.

2. ETG turbulence

Simulations were carried out using the flux-tube gyrokinetic δf -PIC code, PG3EQ [10], using the same physical parameters as in [3, 4, 18], as well as with $r/R = 0$. (We refer to these parameters as ‘Cyclone like,’ since they match those used in the ‘Cyclone’ study reported in [18]). Both sets of simulations reproduce the key features of the results reported in [3, 4] including (1) the first nonlinear-saturation peak in χ_e , (2) the rise after this peak shown in figure 4 of [4], (3) the low late-time value of χ_e ($\chi_e \approx 3\chi_{eGB}$ for $r/R = 0.18$ and $\chi_e \approx 1.5\chi_{eGB}$ for $r/R = 0$) and (4) the downshift in wave number of the nonlinear spectrum relative to the linear spectrum [4]. Thus, global effects and the parallel nonlinearity [16, 17] are eliminated as the cause of the discrepancy between [1] and [3]. The removal of trapped particles (setting $r/R = 0$) does not significantly change the time dependence of χ_e nor its value in the late-time low- χ_e state.

We have shown [5], however, that in this low- χ_e state in both these PG3EQ simulations and those reported in [3, 4], discrete particle noise has become large enough to suppress the physical ETG turbulence. Since discrete particle noise is a numerical artefact, it cannot be inferred on the basis of the PIC simulations of [3, 4] that the higher χ_e values given by the continuum-code simulations of [1, 2] are incorrect. Other simulation studies [19, 20] have shown that global PIC gyrokinetic codes can reproduce the higher χ_e values of [1, 2], provided that care is taken to monitor and manage the simulation noise.

The demonstration that the late-time low- χ_e state in the δf -PIC Cyclone-like ETG simulations is a result of discrete particle noise was facilitated by the development of a theoretical model of the interaction of δf -PIC simulation noise and physical turbulence [5]. This model reproduces the behaviour of noise-affected gyrokinetic δf -PIC simulations of both ETG turbulence, in which the noise suppresses the turbulence, and ITG turbulence, where the noise and turbulence coexist and both contribute to the net transport. A key component of this model is a detailed theoretical result for the spectrum of electrostatic potential noise fluctuations in a δf gyrokinetic particle simulation. This result is based on Krommes’ calculation of the gyrokinetic noise spectrum [22], extended to include the effects of numerical filtering and finite-size, weighted particles. Spectra from the late-time, low- χ_e phase of the Cyclone-like δf -PIC ETG simulations show excellent agreement with this noise-based result, indicating that at that time, these simulations are dominated by noise.

We have also shown directly [5] that simulation noise can reduce the linear growth of or completely stabilize the physically unstable ETG modes. Furthermore, the time of maximum amplitude of each mode in our nonlinear δf -PIC Cyclone-like ETG simulations coincides with the time at which its linear growth rate, as modified by the noise diffusion, goes from positive to negative. This strongly suggests that

this stabilization is the cause of suppression of the turbulent transport in these simulations.

Gyrokinetic simulation codes are subject to various discretization errors in addition to the simulation noise exhibited by PIC codes. In continuum codes discretization errors in the numerical advection scheme may result in dispersion errors or dissipation that could result in errors in real frequencies or growth rates of modes, and errors in the balances in the nonlinear phase. Careful choices of the phase space meshing can minimize advection related errors by ensuring as much as possible that the mesh is aligned with the directions of advection (e.g. by using coordinates based on constants of the motion or adiabatic invariants [23]). In contrast to the noise in the δf -PIC simulations of [3–5], these errors are not expected to have a secularly growing impact on the dynamical balances in the nonlinear states. The effects of these discretization errors on the linear growth rates in continuum codes have been checked (see [1, 2] and references therein, and [23, 24]). The need to check that the simulations have successfully reduced these errors to acceptable levels in the nonlinear states motivates nonlinear benchmarks. We therefore undertook a successful inter-code benchmark [6] involving the continuum gyrokinetic codes GYRO [23], GS2 [1, 2], and GENE [1, 2], and the δf -PIC code PG3EQ [10]. Because all of these codes show strong sensitivity of the results to numerical parameters at the physical plasma parameters used in [3, 4], this benchmark was undertaken at an alternate reference point, magnetic shear $s = 0.1$ instead of $s=0.796$. This change produces a large (two orders of magnitude) drop in the heat transport even though the change in the linear growth spectrum is modest. Good agreement was achieved by several measures, with the time-interval weighted standard deviation in $\langle \chi_e \rangle$ between codes less than that achieved in the Cyclone ITG benchmarking exercise [18].

Scans in the magnetic shear [6] show that as the magnetic shear is increased over the range $0.1 \leq s \leq 0.35$ average of χ_e undergoes only a modest change, from 2.7 to $3.8\chi_{eGB}$. When the magnetic shear is increased further to $s = 0.4$ the electron thermal conductivity takes a dramatic jump to $\langle \chi_e \rangle = O(100) \times \chi_{eGB}$. In simulations with PG3EQ at $s = 0.4$ the heat flux rises to track the results from GYRO and GENE before simulation noise suppresses the turbulence.

The magnetic shear scan was repeated, employing GYRO, with the adiabatic ions replaced by full gyro-kinetic ions at a mass ratios of $m_i/m_e = 400$ and 600, with a somewhat larger flux-tube cross-section, $256\rho_e \times 128\rho_e$. With kinetic ions the electron heat flux settles down to a modest late-time average value, in the range 10–14 χ_{eGB} .

Transport analyses of DIII-D [26], JET [27], JT-60U [28], and NSTX [29] discharges yield χ_e/χ_{eGB} values in the range of 1 to (usually somewhat less than) 25. This is consistent with our ETG simulation results and suggests that ETG turbulence may be responsible for the electron heat transport across thermal barriers and in the L-mode edge of discharges with internal transport barriers.

3. ITG turbulence: sources and sinks of zonal flow

The development of the zonal-flow-balance diagnostic for gyrokinetic simulations (of ITG turbulence) proceeds by

writing an equation for the rate of change of the zonal-flow $E \times B$ shear V'_{EB} :

$$\frac{\partial V'_{EB}}{\partial t} \propto \frac{\partial \langle n_{gi} \rangle_{fs}}{\partial t} = \left\langle \int B d\mu dv_{||} d\theta \frac{\partial \delta f_g(x - \rho \hat{\rho}_x)}{\partial t} \right\rangle_{fs}. \quad (1)$$

Here, n_{gi} is the gyrocentre density δf_g is the perturbed ion gyrocentre distribution, t is the time, B is the magnetic field, μ is the magnetic moment, $v_{||}$ is the parallel velocity, θ is the gyrophase angle, x is the real-space radial position, ρ is the gyroradius, $\hat{\rho}_x$ is the radial component of the gyroradius unit vector and $\langle \cdot \rangle_{fs}$ denotes a flux surface average. Note that this relationship is accurate to second order in the gyroradius, as are typical finite-Larmor-radius fluid models (e.g. that of [30]). Higher order terms could be kept if desired either by the insertion of a suitable Padé-based operator (which can be implemented using tridiagonal matrix inversions, as is already done in the zonal field-solver in the PG3EQ code [10]), or simply by viewing $\langle n_{gi} \rangle_{fs}$ as a useful generalized vorticity quantity given by a positive self-adjoint integral operator acting on $\langle \phi \rangle_{fs}$. Upon replacement of $\partial \delta f_g / \partial t$ using the nonlinear gyrokinetic equation [31, 10], each term therein yields a contribution to $\partial V'_{EB} / \partial t$ that can be identified as a source or sink of zonal flow or zonal flow shear.

The terms associated with the radial gyroaveraged $E \times B$ drift flow \bar{V}_{EBx} can be further decomposed. Thus,

$$\frac{\partial}{\partial x} \left\langle \int B d\mu dv_{||} d\theta V_{EBgx} \delta f_g(x - \rho \hat{\rho}_x) \right\rangle_{fs}, \quad (2)$$

where V_{EBgx} is the radial $E \times B$ drift at the gyrocentre, can be identified as the Reynolds' stress. The related term

$$\frac{\partial}{\partial x} \left\langle \int B d\mu dv_{||} d\theta (\bar{V}_{EBx} - V_{EBgx}) \delta f_g(x - \rho \hat{\rho}_x) \right\rangle_{fs}, \quad (3)$$

where \bar{V}_{EBx} is the gyroaveraged radial $E \times B$ drift, can be identified with the diamagnetic Reynolds' stress [32, 33]. There are several linear terms. One class of terms can be viewed as the divergences of the perturbed ∇B and curvature-drift flows (magnetic pumping) or (with the addition of appropriate magnetization currents) the perturbed diamagnetic and neoclassical fluid flows

$$\frac{\partial}{\partial x} \left\langle \int B d\mu dv_{||} d\theta (V_{\nabla Bx} + V_{cx}) \delta f_g(x - \rho \hat{\rho}_x) \right\rangle_{fs}. \quad (4)$$

Here, $V_{\nabla Bx}$ and V_{cx} are the radial components of the ∇B and curvature drifts. Additionally, there are terms for which the gyrocentre density change can be thought of as due the compression of the $E \times B$ drift.

$$\frac{\partial}{\partial x} \left\langle \int B d\mu dv_{||} d\theta (V_{\nabla B} + V_c) \cdot \nabla \phi(x - \rho \hat{\rho}_x) F_M \right\rangle_{fs}. \quad (5)$$

In the case of the ∇B -drift term, this compression is in the direction of ∇B due to the decrease in the $E \times B$ drift as B increases. In the case of the curvature drift, this compression is due to the convergence of an $E \times B$ drift across a curved magnetic field. Here ϕ is the electrostatic potential, and F_M is the equilibrium distribution. These terms are nonzero as a result of the velocity dependences of the ∇B and curvature

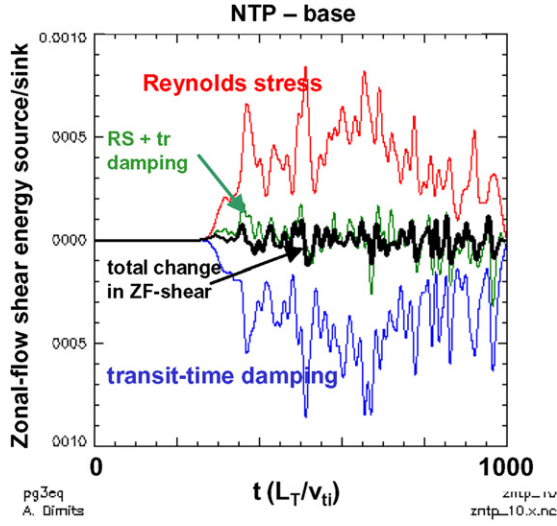


Figure 1. Relative contributions to $\partial\langle|V'_{EB}|^2\rangle_x/\partial t$ from a PG3EQ simulation using the NTP base case parameters. The red curve is the Reynolds stress and linear terms and the black curve is the total rate of change of $\langle|V'_{EB}|^2\rangle_x$.

drift flows. The above decomposition results in an equation of the form

$$\frac{\partial V'_{EB}}{\partial t} \approx \sum_i R_i. \quad (6)$$

To facilitate analysis, it is helpful to recast this as an equation for a positive definite scalar quantity. One choice is $\langle|V'_{EB}|^2\rangle_x$, where $\langle\rangle_x$ represents a radial average, which is the enstrophy associated with the zonal $E \times B$ flow. The resulting equation is

$$\frac{\partial\langle|V'_{EB}|^2\rangle_x}{\partial t} \approx 2 \sum_i \langle R_i V'_{EB} \rangle_x. \quad (7)$$

Alternatively, the zonal-flow energy $\langle|V_{EB}|^2\rangle_x$ can be used. It can be shown that (e.g. it follows rigorously from the exact form of the gyrokinetic Poisson equation or from the Padé approximation used in PG3EQ [10]) that $\langle\phi n_{gi}\rangle_x$ is positive definite. This leads to a useful approximate equation for the zonal-flow energy:

$$\frac{\partial\langle|V_{EB}|^2\rangle_x}{\partial t} \approx 2 \sum_i \langle\phi R_i\rangle_x. \quad (8)$$

Each of the R_i s contributes a term in equation (7) or (8), and is calculated as a profile on the radial mesh in PG3EQ through suitable ‘particle deposition’ operations. The resulting contributions to $\langle|V'_{EB}|^2\rangle_x$ in equation (7) or $\langle|V_{EB}|^2\rangle_x$ in equation (8) are then calculated as a postprocess using the GKV analysis package [5] (and the profile of δn_{gi} or ϕ .) It has been carefully verified that the resulting terms do indeed satisfy equation (6) to good accuracy (i.e. that the accumulated R_i terms add to the directly calculated values of $\partial V'_{EB}/\partial t$), and consequently also satisfy equations (7) and (8).

Figure 1 shows the results of applying this diagnostic to the calculation of the terms in equation (7) for a PG3EQ simulation using the parameters of [34], with the adiabatic-electron model of [35] (also used in [8, 9]). (The terms of equation (8) have also been examined and yield qualitatively similar conclusions

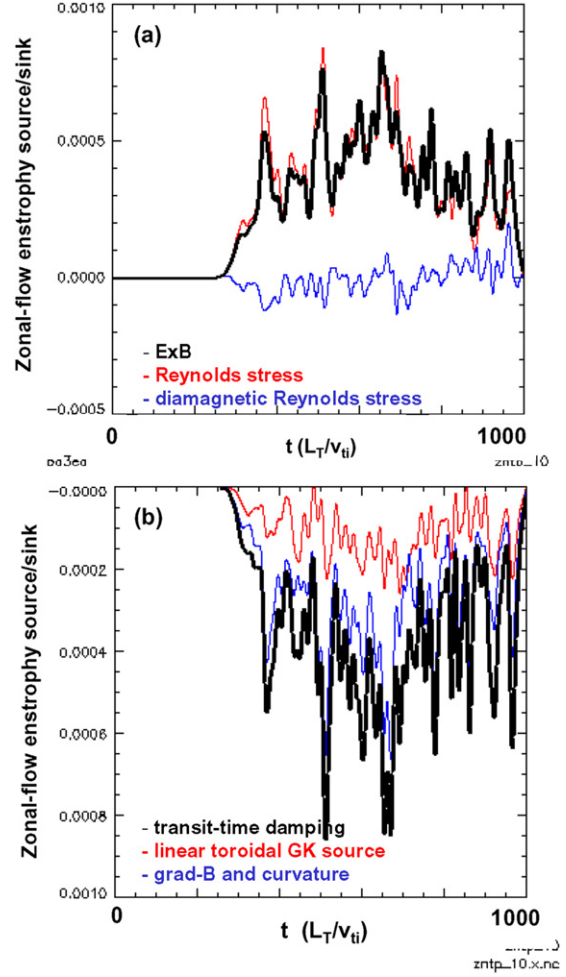


Figure 2. Further decompositions of the sources (a) and sinks (b) of zonal-flow enstrophy $\langle|V'_{EB}|^2\rangle_x$ from the simulation shown in figure 1.

to those for equation (7).) The Reynolds stress contribution (equation (2)) is seen to be positive definite and is the main source of zonal flow shear. The linear terms (equations (4) and (5)), the sum of which is the blue curve, act as sinks. The total rate of change of $\langle|V'_{EB}|^2\rangle_x$ is shown as the black curve, while the green curve is the sum of just the Reynolds stress of equation (2) and linear terms of equations (4) and (5). That the green curve tracks the black curve well indicates that the Reynolds stress and linear terms capture most of the contribution. The net imbalance in the early time ($t = 200$ – 300) variation is associated with the initial buildup of the zonal flow. It is clear from the figure that the Reynolds stress and linear damping terms are each much larger than the net rate of change of $\langle|V'_{EB}|^2\rangle_x$, which is the small residual difference between these two terms.

The sources and sinks are further decomposed in figure 2. The diamagnetic-Reynolds-stress contribution (equation (3)) is found to be small and acts as a weak sink. The linear damping terms have comparable contributions from the magnetic pumping terms (equation (4)) and the $E \times B$ -compression terms (equation (5)). This diagnostic has been applied to, and the same conclusions reached for, a variety of PG3EQ simulation cases, including several points

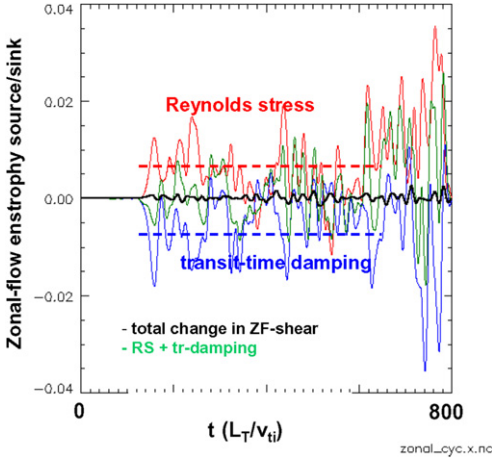


Figure 3. Relative contributions to $\partial(|V'_{EB}|^2)_x/\partial t$ from a simulation using the same parameters as in figure 1, but with the quantities calculated by sampling at four poloidal locations (outer and inner midplane and top and bottom).

in temperature-gradient scans about the Cyclone parameter set [18] and the ‘NTP’ parameter set [34].

We note that the present diagnostic does not distinguish between the zero-frequency zonal-flow and geodesic-acoustic-mode (GAM) contributions (see, e.g., [14]). In the future, we plan to extend these calculations to the first sinusoidal components (in poloidal angle) of relevant fields and flows. It is seen from figures 1 and 2 that the Reynolds stress source has a significant steady mean squared value in addition to the fluctuating component. The linear collisionless damping present in these simulations (represented by equations (4) and (5)) acts through the GAMs only. The zero-frequency component is undamped (as was verified in e.g., [18]). The decay of the zonal flows likely has a nonlinear component associated with tertiary instabilities. The present diagnostic does not extract this effect, but lumps it in with the Reynolds stress sources of equations (2) and (3).

We have also extended this analysis to provide guidance for experimental fluctuation diagnostics, which are typically able to measure fluctuations in a spatially localized region rather than an entire flux surface or even a flux-surface ring (spanning a poloidal circuit and a small range of toroidal angle). It is found that 4 poloidally localized samples are sufficient, and appear to be necessary, to provide a resolution of the zonal-flow shear sources and sinks. An example of this is shown in figure 3. Using 8 poloidal samples improves the quality of the time traces of the sources and sinks over 4 samples. Attempts have been made with 2 poloidally localized samples at various poloidal locations. These give traces for either the net linear or nonlinear contribution, or both, that do not have a measurably nonzero average.

Some interesting results have been obtained from investigations of zonal-flow dynamics and the application of the above diagnostic to ETG turbulence simulations (carried out with PG3EQ): (1) In the Cyclone-like $s = 0.8$ cases in which the transport rises to large values, it has been found that this tendency for χ_e to rise to large values goes away if the zonal potential ($E \times B$ flow) is removed. The cause of this counterintuitive result is under investigation. (2) Restarts during the χ_e rise phase with the zonal potential set to zero result in

a cessation of the rise. (3) For the $s = 0.1$ benchmark case, which does reach a reasonably robust steady state, the zonal-flow balance dynamics differs significantly from that in ITG simulations. The Reynolds stress is still found to be a source, but it is compensated by the diamagnetic Reynolds stress so that the net contribution of the gyroaveraged $E \times B$ drift

$$\frac{\partial}{\partial x} \left\langle \int B \, d\mu \, dv_{\parallel} \, d\theta \, \bar{V}_{EBx} \, \delta f_g(x - \rho \hat{\rho}_x) \right\rangle_{fs}$$

is small. Additionally, the compression of the radial ∇B and curvature-drift fluxes (equation (4)) acts as a source, while the linear toroidal compression term (equation (5)) acts as a sink of zonal flow energy and enstrophy. The linear terms negate each other as do the nonlinear terms.

4. ITG turbulence: real-geometry-tokamak gyrokinetic simulations

SUMMIT/PG3EQ_NC is a nonlinear δf -PIC gyrokinetic code which implements real geometry using the quasi-ballooning representation [10] of the field quantities. It has been interfaced to DIII-D equilibrium analyses from the EFIT [36], ONETWO [37] and PLOTEQ [38] codes.

Verification of PG3EQ_NC has been carried out by comparing it in detail to the earlier circular-cross-section gyrokinetic code PG3EQ [10]. Agreement with roundoff for many time steps, and across different parallel domain decompositions has been obtained when the initial loading and equilibrium are identical.

Real-geometry PG3EQ_NC simulations have been undertaken of toroidal ITG instability growth and turbulence using equilibria from several DIII-D shots including shots #81499 and #118561. The electrons were treated with the adiabatic-electron model [8, 9, 35]. Simulations using ‘circularized’ equilibria with parameters set to the radially local poloidally averaged values or appropriate sinusoidal approximations from the actual equilibria are also shown below and discussed for comparison. This circular-equilibrium approximation is discussed in [18], in which a circularized version of DIII-D shot #81499 was used as the basis for the ‘Cyclone’ ITG turbulence simulation comparison. Shot #118561 was part of a recent DIII-D campaign in which broad wavenumber range density fluctuation measurements were performed. This range includes wavenumbers from ~ 0.7 to 35 cm^{-1} ($k\rho_s \approx 0.2\text{--}10$), covering the range of ITG and ETG instabilities. Plasma instabilities were excited by using short duration neutral beam blips to modify the plasma parameters from a low-transport ohmic state. These perturbations modified the background temperature and density as well as the density fluctuation behaviour. The measured response to these perturbations varied with wavenumber, supporting the need for broad wavenumber comparisons including both the ITG and ETG range of wavenumbers.

Figure 4 shows the time history of the ion thermal transport and images of the electrostatic potential ϕ on a poloidal section from the ITG simulations using PG3EQ_NC and equilibria from EFIT and ONETWO analyses for shot #81488 at $t = 4000 \text{ ms}$. These simulations show the expected linear ITG instability growth and saturation. The maximum linear growth

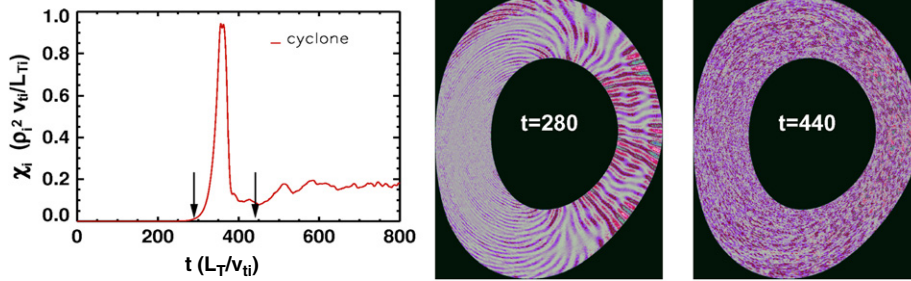


Figure 4. Time history of χ_i and images of the electrostatic potential in a poloidal section from a PG3EQ_NC simulation using a real DIII-D equilibrium from EFIT and ONETWO analyses of shot #81499 at $t = 4000$ ms, and $r/a = 0.509$. The simulation times for the electrostatic potential plots in the simulation are $t = 280$ and $440 L_{Ti}/c_s$.

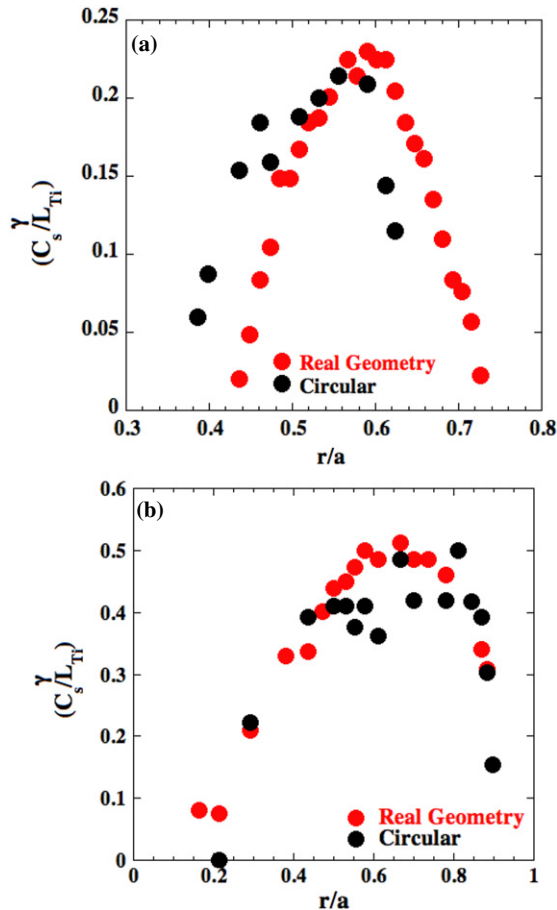


Figure 5. Maximum ITG growth rates (in units of c_s/L_{Ti}) versus minor radius from PG3EQ_NC simulations using real DIII-D equilibria (red) and circularized equilibria (black) from (a) shot #81499 at $t = 4000$ ms and (b) shot #118561 at $t = 1450$ ms.

rate for the case shown in figure 4 is very close to that for the corresponding circularized case (figure 5(a) at $r/a = 0.5$), while the late-time ion thermal transport level is reduced to less than half of that for the circularized case. This case was run with a 128×128 (perpendicular) $\times 64$ mesh, with an outboard-midplane perpendicular grid cell size of $0.9817 \rho_i$, and 16 particles per cell. Convergence tests indicated that higher parallel resolution is needed for the noncircular case than for the corresponding circularized cases, primarily because of the somewhat sharper poloidal variation of the local magnetic shear and the curvature components as a function

of poloidal angle. This sharper variation leads to stronger poloidal localization of the turbulence, which may be a key factor in the reduction of χ_i . The zonal-flow intensity and mean shearing rate undergo a modest reduction (a factor of 0.6–0.8), so it appears unlikely that the change in the zonal flow properties is a cause of the reduction in χ_i .

Figure 5 shows profiles of maximum ITG growth rates versus minor radius from PG3EQ_NC simulations using real DIII-D equilibria and circularized equilibria from shot #81499 and shot #118561. There is some jumpiness in the growth-rate profiles for the circular-geometry cases, which is present because the box size was not optimized for every case to capture the most unstable mode exactly. Despite this variability in the circular cases, some conclusions can be drawn. The shot-#81499 cases show a modest systematic effect of shaping, with the real-geometry growth-rate profile $\gamma(r)$ shifted slightly outwards relative to the circular case. The shot #118561 cases show very little effect of shaping on the maximum growth rates. Examination of the local equilibrium parameters indicates that the toroidal ITG modes become stable at large minor radius primarily because the magnetic shear becomes large. At small minor radius, the growth rates become small because the temperature gradient becomes small, causing the dimensionless parameters R/L_{Ti} and $\eta_i = L_{ni}/L_{Ti}$, where L_{ni} is the ion density gradient scale length, to fall below marginal values.

Presently being undertaken are (a) a comparison of these $\gamma(r)$ profiles with results from the GKS code [31], and (b) larger nonlinear simulation runs that will yield χ_i profiles for both of the discharges studied here.

5. Summary and conclusions

We have reported progress on understanding three aspects of ETG and ITG turbulence obtained using nonlinear gyrokinetic simulations.

We have carried out an investigation, using both PIC and continuum simulations as well as analytical theory, of the discrepancy between previous continuum-code [1, 2] and global-PIC [3, 4] gyrokinetic simulations of ETG turbulence. This investigation strongly supports the conclusions of the earlier continuum-code simulations, that levels of the electron thermal conductivity χ_e are large enough to be significant in some tokamaks.

A successful benchmark between PIC and continuum codes for ETG turbulence has been completed. Because both

PIC- and continuum-code ETG simulations at the plasma parameters used in [1, 2] and [3, 4] produce very large intermittent transport and strong sensitivity of the results to numerical parameters, this benchmark was undertaken at an alternate reference point, magnetic shear $s = 0.1$, instead of $s = 0.796$. At this more tractable benchmark point, good agreement was achieved, with the time-interval weighted standard deviation in $\langle\chi_e\rangle$ between codes yielding an error in our estimate of the mean of less than 10%. This is better than was achieved in the Cyclone ITG benchmarking exercise [18]. Scans in the magnetic shear show an abrupt transition to a high- χ_e state as the shear is increased above $s = 0.4$, and good agreement between codes in tracking this trend. When nonadiabatic ions are used, this abrupt transition is absent, and χ_e increases gradually reaching values consistent with transport analyses of DIII-D, JET, JT60-U and NSTX discharges.

The balances of zonal-flow driving and damping terms in late-time quasi-steady phase have been unfolded using a new run-time gyrokinetic-simulation diagnostic. This investigation contrasts with most previous zonal-flow generation and damping studies, which mostly addressed either the early-time onset of the zonal flows or otherwise transient behaviour evolving from a simplified initial state, and is important because zonal flows play a key role in regulating toroidal ITG turbulence and transport in the nonlinear phase of the simulations. The zonal flow level is set by a balance of large driving and damping terms which almost cancel each other. The driving of the zonal flows was found to be mostly by the Reynolds' stress, while the dissipation is mostly by the linear (transit-time) damping terms. An issue affecting the viability of applying such a diagnostic directly to experimental data has been addressed by showing that in the simulations, useful zonal-flow-balance information can be obtained with spatially localized samples at as few as four poloidal locations.

Finally, studies of the effect of real geometry on ITG turbulence using SUMMIT/PG3EQ_NC, a real-geometry version of our nonlinear δf -PIC gyrokinetic code PG3EQ, were reported. Real DIII-D equilibrium reconstruction data from EFIT, ONETWO and PLOTEQ-code analyses are used. The simulations completed so far show modest effects of real geometry on the maximum linear growth rate profiles, but some reduction in the thermal transport levels in the late-time nonlinear state compared with the circularized cases.

Acknowledgments

The authors would like to thank B. Cohen, K. Hallatschek, W.W. Lee, Z. Lin, S. Parker, B. Scott, E.J. Synakowski, M. Umansky and X.Q. Xu for useful discussions, and H. St John for his help with the PLOTEQ code. This work was performed for US DOE at U.C. LLNL under Contract No W7405-ENG-48, at PPPL under Contract No DE-AC02-76CH03073, U. Maryland under Grant No DE-FG02-93ER54197, UCLA under Grant No DE-FG02-04ER54740 and at General Atomics under Contract Nos DE-FG03-95ER54309 and DE-FG02-92ER54141. Some of the simulations described here made use of resources at the National Energy Research Supercomputer Center under Department of Energy Contract No DE-AC03-76SF00098.

References

- [1] Jenko F., Dorland W., Kotschenreuther M. and Rogers B.N. 2000 *Phys. Plasmas* **7** 1904
- [2] Dorland W., Jenko F., Kotschenreuther M. and Rogers B.N. 2000 *Phys. Rev. Lett.* **85** 5579
- [3] Lin Z. *et al* 2005 Electron thermal transport in tokamaks: ETG or TEM turbulence *Proc. 20th Int. Conf. on Fusion Energy 2004 (Vilamoura, 2004)* (Vienna: IAEA) CD-ROM file TH/8-4 and <http://www-naweb.iaea.org/napc/physics/fec/fec2004/datasets/index.html>
- [4] Lin Z. *et al* 2005 *Phys. Plasmas* **12** 056125
- [5] Nevins W.M., Hammett G.W., Dimits A.M., Dorland W. and Shumaker D.E. 2005 *Phys. Plasmas* **12** 122305
- [6] Nevins W.M. *et al* 2006 *Phys. Plasmas* **13** 122306
- [7] Luce T.C. *et al* 1995 *Proc. 15th Int. Conf. on Plasma Physics and Controlled Nuclear Fusion Research 1994 (Seville, 1994)* vol 1 (Vienna: IAEA) p 319
- [8] Hammett G.W., Beer M.A., Dorland W., Cowley S.C. and Smith S.A. 1993 *Plasma Phys. Control. Fusion* **35** 973–85
- [9] Dimits A.M. *et al* 1995 *Proc. 15th Int. Conf. on Plasma Physics and Controlled Nuclear Fusion Research 1994 (Seville, 1994)* vol 3 (Vienna: IAEA) p 457
- [10] Dimits A.M., Williams T.J., Byers J.A. and Cohen B.I. 1996 *Phys. Rev. Lett.* **77** 71
- [11] Chen L., Lin Z. and White R. 2000 *Phys. Plasmas* **7** 3129–32
- [12] Rogers B.N., Dorland W. and Kotschenreuther M. 2000 *Phys. Rev. Lett.* **85** 5336
- [13] Scott B. 2003 *Phys. Lett. A* **320** 53
- [14] Hallatschek K. and Zeiler A. 2000 *Phys. Plasmas* **7** 2554–64
- [15] Lin Z., Hahm T.S., Lee W.W., Tang W.M. and Diamond P.H. 1999 Effects of collisional zonal flow damping on turbulent transport *Phys. Rev. Lett.* **83** 3645–8
- [16] Lee W.W., Ethier S., Wang W.X., Tang W.M. and Klasky S. 2006 *J. Phys. Conf. Ser.* **46** 73–81
- [17] Candy J., Waltz R.E., Parker S.E. and Chen Y. 2006 *Phys. Plasmas* **13** 074501
- [18] Dimits A.M. *et al* 2000 *Phys. Plasmas* **7** 969
- [19] Idomura Y., Tokuda S. and Kishimoto Y. 2005 Global profile effects and structure formations in toroidal electron temperature gradient driven turbulence *Nucl. Fusion* **45** 1571–81
- [20] Bottino A., Peeters A.G., Hatzky R., Joliet S., McMillan B.F., Tran T.M. and Villard L. 2007 Nonlinear low noise particle-in-cell simulations of electron temperature gradient driven turbulence *Phys. Plasmas* **14** 010701
- [21] Lee W.W. *et al* 2006 Long time simulation of microturbulence *Proc. 21st Int. Conf. on Fusion Energy 2006 (Chengdu, 2006)* (Vienna: IAEA) CD-ROM file TH/2-6Rb and <http://www-naweb.iaea.org/napc/physics/FEC/FEC2006/html/index.htm>
- [22] Krommes J.A. 1993 *Phys. Fluids B* **5** 1066
- [23] Candy J. and Waltz R.E. 2003 *J. Comput. Phys.* **186** 545
- [24] Kotschenreuther M., Rewoldt G. and Tang W.M. 1995 *Comput. Phys. Commun.* **88** 128
- [25] Candy J. and Waltz R.E. 2006 Coupled ITG/TEM-ETG gyrokinetic simulations *Proc. 21st Int. Conf. on Fusion Energy 2006 (Chengdu, 2006)* (Vienna: IAEA) CD-ROM file TH/2-1 and <http://www-naweb.iaea.org/napc/physics/FEC/FEC2006/html/index.htm>
- [26] Stallard B.W. *et al* 1999 *Phys. Plasmas* **6** 1978
- [27] Parail V.V. *et al* 1999 *Nucl. Fusion* **39** 429
- [28] Shirai H. *et al* 1999 *Nucl. Fusion* **39** 1713
- [29] LeBlanc B.P. *et al* 2004 *Nucl. Fusion* **44** 513
- [30] Braginskii S.I. 1965 Transport properties in a plasma *Reviews of Plasma Physics* ed M.A. Leontovich (New York: Consultants Bureau) vol 1 p 205–311
- [31] Frieman E. and Chen L. 1982 *Phys. Fluids* **25** 502

- [32] Horton W., Estes R.D. and Biskamp D. 1980 *Plasma Phys.* **22** 663
- [33] Smolyakov A.I., Diamond P.H. and Medvedev M.V. 2000 *Phys. Plasmas* **7** 3987
- [34] Cohen B.I. *et al* 1995 *Comput. Phys. Commun.* **87** 1
- [35] Cohen B.I., Williams T.J., Dimits A.M. and Byers J.A. 1993 *Phys. Fluids B* **5** 2967
- [36] Lao L.L., St John H., Stambaugh R.D., Kellman A.G. and Pfeiffer W. 1985 *Nucl. Fusion* **25** 1611
- [37] Pfeiffer W.W., Davidson R.H., Miller R.W. and Waltz R.E. 1980 ONETWO: A computer code for modeling plasma transport in tokamaks *General Atomics Report* GA-A16178
- [38] St John H. 2004 private communication